Supporting Information

Phase-engineering of nickel hydroxide in Ni/Ni(OH)$_2$ interface for efficient hydrogen evolution and hydrazine-assisted water splitting in seawater

Duo Shao,[§,a] Qi Wang,[§,a] Xianzhi Yao,[c] Yitong Zhou,[,a] and Xin-Yao Yu*[,a,b]*

[a]Institutes of Physical Science and Information Technology, Anhui University, Hefei 230601, P. R. China

[b]School of Materials Science and Engineering, Anhui University, Hefei 230601, P. R. China

[c]Ningbo Research Institute of Ecological and Environmental Sciences, Ningbo 315000, P. R. China

*Email: yuxinyao@ahu.edu.cn (X.Y.Y.) and zhouyt@ahu.edu.cn (Y.Z.)

[§]D.S. and Q.W. contributed equally to this work.

Experimental section

Chemicals: Ni foam with a thickness of 1.5 mm was obtained from GJY Electron. Mater. Co., Ltd. Nickle nitrate hexahydrate ($Ni(NO_3)_2 \cdot 6H_2O$) were obtained from Aladdin reagent Co., Ltd. Urea (CH_4NO_2), ammonium fluoride (NH_4F), sodium hydroxide (NaOH), potassium hydroxide (KOH), and hydrochloric acid (HCl) were supplied by Sinopharm Chemical reagent Co., Ltd. Pt/C (platinum, 20% on carbon) was obtained from Alfa Aesar. Hydrazine hydrate 80% was purchased from Tianjin Fengchuan Chemical Reagent Technology Co. LTD. All of the chemicals were used as received without further purifications. Deionized water with the resistance of 18.25 MΩ·cm at room temperature was used to prepare the aqueous solution. The seawater used in this work is real seawater from Qingdao, China. It is mainly composed of NaCl, $MgCl_2$, $MgSO_4$, and K_2SO_4. The alkaline seawater electrolyte was prepared by mixing KOH solution with natural seawater and the pH of the mixed electrolyte was adjusted to 14. There was no other pre-treatment of the natural seawater and the electrochemical testing in 1 M KOH seawater electrolyte was performed after most of the visible particles settled down.

Synthesis of α-Ni(OH)₂ NSAs: Firstly, Ni foam with a size of 2*3 cm^2 was sonicated in ethanol and 2 M HCl for 5 min and 15 min, respectively, to remove the nickel oxides on the surface, rinsed with deionized water repeatedly, and then dried in oven at 60 °C overnight. In a typical synthesis, 0.4655 g of $Ni(NO_3)_2 \cdot 6H_2O$ and 0.4855 g of urea were dissolved into 40 mL of deionized water followed by stirring for 30 min to achieve the uniform dispersion. The as-prepared solution was then sealed into 50 mL

Teflon-lined stainless steel autoclave. Subsequently, a piece of pretreated Ni foam was immersed into the autoclave and heated at 120 °C for 2 h. After reaction, the resultant Ni foam was taken out and washed with deionized water for several times.

Synthesis of β-Ni(OH)$_2$ NSAs: The synthesis of β-Ni(OH)$_2$ nanosheets is based on a simple two-step hydrothermal method. The first hydrothermal procedure was similar to that of α-Ni(OH)$_2$ nanosheets, except adding 0.1185 g of NH$_4$F into the system. And then, the as-prepared precursor was put into 0.1 M NaOH aqueous solution and transferred into a 50 mL Teflon autoclave for hydrothermal reaction at 180 °C for 2 h. After that, the resultant sample was rinsed with water for a few times and dried at 60 °C.

Synthesis of Ni/α-Ni(OH)$_2$ and Ni/β-Ni(OH)$_2$ NSAs: The α-Ni(OH)$_2$ or β-Ni(OH)$_2$ NSAs loaded on Ni foam was fixed on the Teflon base in a low-temperature radio frequency (RF) plasma device and activated by using pure H$_2$ plasma with 400 W of power, 40 Pa of gas pressure, and 20 min activation time to obtain Ni/α-Ni(OH)$_2$ or Ni/β-Ni(OH)$_2$ NSAs.

Synthesis of Pt/C electrode: Commercial Pt/C powder (20 wt%, 5 mg) was dispersed in a mixed solution of ethanol (270 μL), deionized water (200 μL), and Nafion solution (30 μL) and ultrasonized for 30 minutes. Then, the mixture was piped onto NF and dried for use. The typical mass loading of Pt/C was 1.2 mg·cm^{-2}.

Structural characterizations: The micro-structural and morphological details of the samples were investigated by field-emission scanning electron microscope (Hitachi S4800) and transmission electron microscope (JEM-2100F). The crystal structure was

characterized by power X-ray diffraction (XRD, DX-2700). The valence state of elements were obtained by X-ray photoelectron spectroscopy (XPS, ESCALAB-MKII spectrometer). C 1s peak at 284.6 eV was used to calibrate all XSP spectra. The generated amounts of H_2 is measured by gas chromatography (GC9790). The optical signal of plasma was recorded by optical emission spectra (OES, PG2000 high speed spectrometer, Idea Optics). Electron spin-resonance (ESR) spectra were recorded on JES FA 300 at room temperature and atmospheric pressure.

Electrochemical characterizations: All the electrochemical measurements were conducted on CHI 760E electrochemical workstation with a typical three-electrode system. An as-prepared samples were directly used as the working electrode, along with a graphite rod as the counter electrode and an Hg/HgO electrode as the reference electrode. The electrolyte was 1.0 M KOH for HER and water electrolysis, while the electrolyte for HzOR is 1.0 M KOH with 100 mM, 200 mM, 300 mM and 400 mM hydrazine. The LSV curves were tested from 0 to -0.5 V *vs.* RHE for HER and 0.3 to -0.1 V *vs.* RHE for HzOR at a scan rate of 1 mV s^{-1} with 90% iR compensation. The AC EIS measurements were collected with frequency ranging from 10^5 to 0.005 Hz. The ECSA was estimated by C_{dl}. Cyclic voltammetry (CV) at different scan rates (20, 40, 60, 80, 100 and 120 mV s^{-1}) in the non-Faradaic region (0.05 to 0.15 V *vs.* RHE) were used to measure C_{dl}. The stability test was measured by chronoamperometry (CA) method at a constant potential. The TOF values are estimated according to the following equation:

$$TOF = \frac{I}{2NF}$$

In which I is current (A) and the F means Faraday constant (96,485 C mol^{-1}). The N is number of active sites which can be calculated with the following equation:

$$N = \frac{Q}{2F} = \frac{It}{2F} = \frac{I \times V/\mu}{2F} = \frac{S}{2F \times \mu}$$

Where S is integrated effective area in CV recorded, and μ is the scan rate (50 mV s^{-1}).

The H$_2$ evolution amount on the Ni/β-Ni(OH)$_2$ nanosheets electrode at 10 mA cm^{-2} is calculated by the following equation:

$$n(H_2)_e = x_0 \times n$$

In which x_0 is the amount of H$_2$ evolution (mol ppm^{-1}) measured by gas chromatography and n is the amount of gas in each vial (1 cm^3). The theoretical amount of H$_2$ evolution during HER is obtained by the equation:

$$n(H_2)_t = \frac{It}{2F}$$

Where I is the measured current (A) and t means time (s) of H$_2$ evolution.

The Faradic efficiency of H$_2$ evolution is calculated according to the following equation: $FE = \dfrac{n(H_2)e}{n(H_2)t} \times 100\ \%$.

Theoretical calculations: All the density functional theory (DFT) were carried out by Vienna ab initio simulation package (VASP).[1-3] The projector augmented-wave (PAW) method was used to describe the core electrons.[4,5] The Perdew-Burke-Ernzerh (PBE) in the generalized gradient approximation (GGA) was applied to describe the exchange-correlation function.[6,7] The plane wave basis with an energy cutoff of 400 eV was applied to expand the valence electrons. The Brillouin zone was sampled with 2×2×1 Monkhorst-Pack k-point mesh, and a Gaussian smearing of 0.05 eV was

applied to speed up electronic convergence. All structures were fully relaxed until the total energy and force convergence criterion was set to 10^{-4} eV and 0.02 eV/Å. The 4×4 supercell of α-Ni(OH)$_2$ and β-Ni(OH)$_2$ nanosheets were used to build the calculation models and 7 Ni atoms nanocluster was combine with Ni(OH)$_2$ nanosheets to build the Ni/Ni(OH)$_2$ models. The water decomposition pathways were obtained using the climbing image nudged elastic band (CI-NEB). A vacuum height of 20 Å along the vertical direction was selected to avoid the unwanted interaction between the slab and its period images. The final structure was illustrated with VESTA software.

The energy of adsorbate M* (ΔE_{M*}) was calculated using the following formula $\Delta E_{M*} = E_{M*} + E_* - E_M$, where E_{M*} and E_* are the DFT calculation energy of adsorption system, unabsorbed surface, and an isolate intermediate M, respectively.
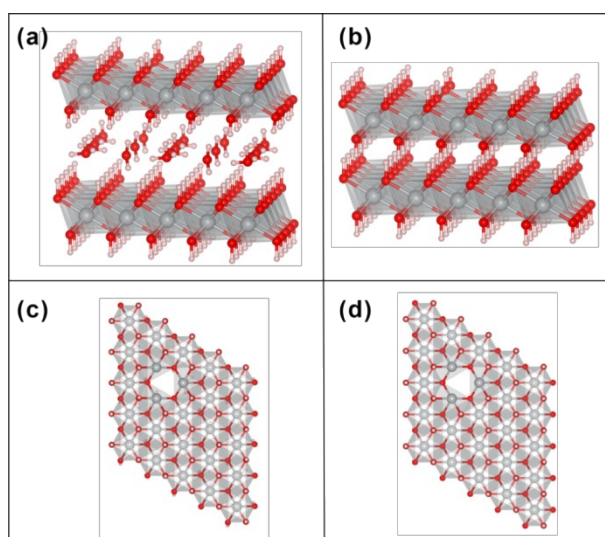
Fig. S1. The side view and top view of the model of α-Ni(OH)$_2$ (a-c) and β-Ni(OH)$_2$ (b-d) with oxygen vacancies. Grey balls: Ni atoms; Red balls: O atoms; Pink balls: H atoms.
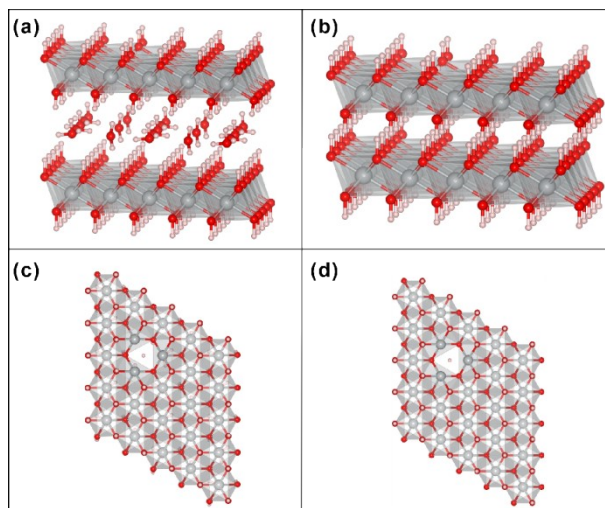
Fig. S2. The adsorption of H on α-Ni(OH)$_2$ (a-c) and β-Ni(OH)$_2$ (b-d). Grey balls: Ni atoms; Red balls: O atoms; Pink balls: H atoms.
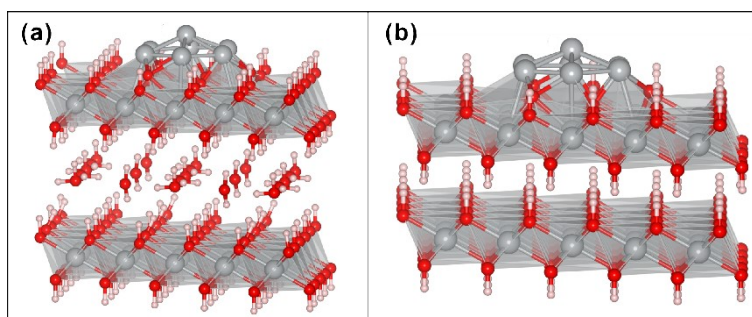
Fig. S3. The side view of the model of Ni/α-Ni(OH)$_2$ (a) and Ni/β-Ni(OH)$_2$ (b). Grey balls: Ni atoms; Red balls: O atoms; Pink balls: H atoms.
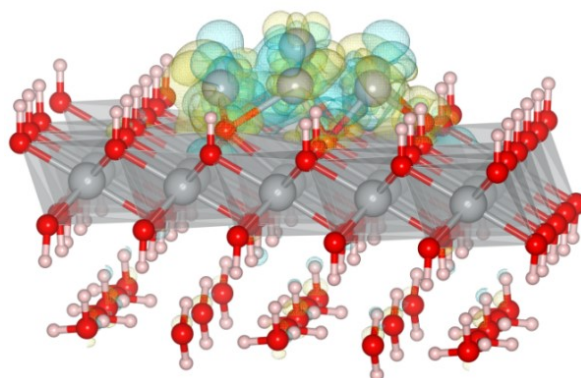
Fig. S4. The charge density difference of Ni/α-Ni(OH)$_2$. Grey balls: Ni atoms; Red balls: O atoms; Pink balls: H atoms. Yellow and cyan clouds indicate charge gain and loss, respectively.
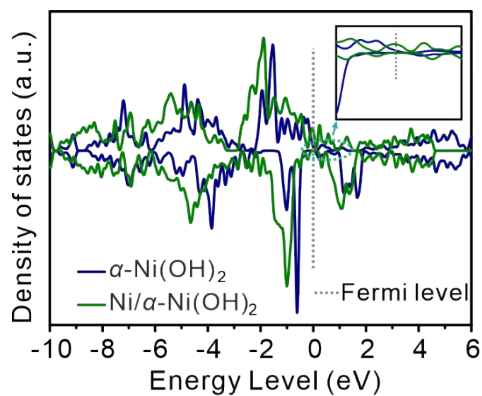
Fig. S5. The DOS plots of α-Ni(OH)$_2$ and Ni/α-Ni(OH)$_2$. The inset is the enlarged plot near the Fermi level.
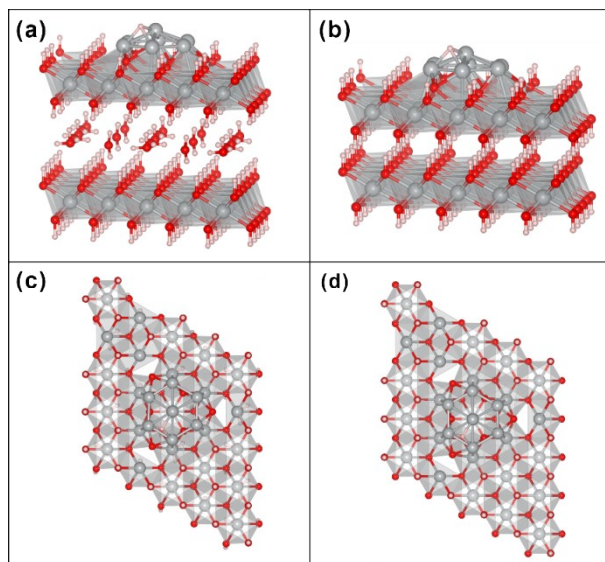
Fig. S6. The adsorption of H on the Ni(0) sites of Ni/α-Ni(OH)$_2$ (a-c) and Ni/β-Ni(OH)$_2$ (b-d). Grey balls: Ni atoms; Red balls: O atoms; Pink balls: H atoms.
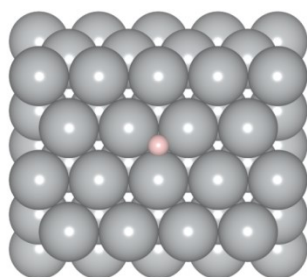
Fig. S7. The adsorption of H on metallic Ni. Grey balls: Ni atoms; Pink balls: H atoms.
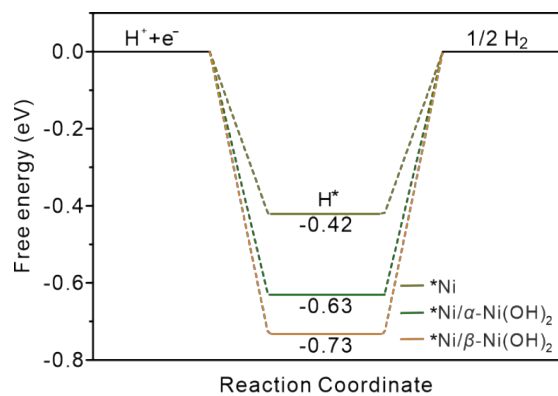
Fig. S8. Free energy diagrams for hydrogen adsorption on metallic Ni and Ni(0) sites of Ni/α-Ni(OH)$_2$ and Ni/β-Ni(OH)$_2$.
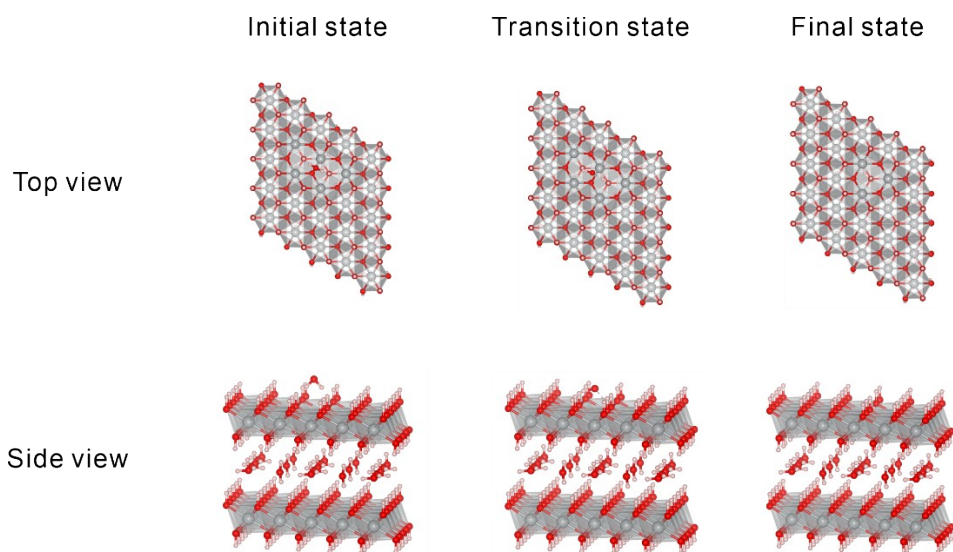
Fig. S9. DFT calculations of initial state (IS), transition state (TS), and final state (FS) for water dissociation on α-Ni(OH)$_2$. Grey balls: Ni atoms; Red balls: O atoms; Pink balls: H atoms.
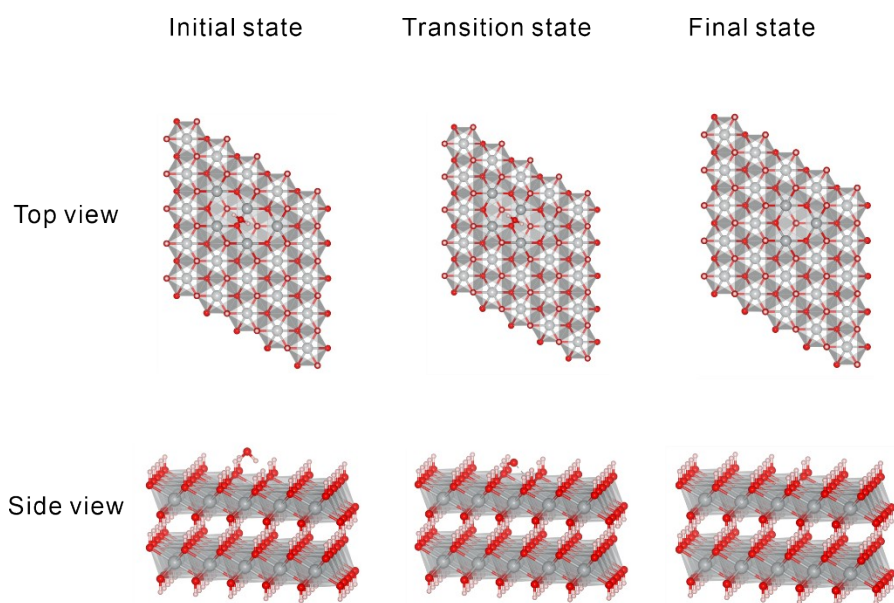
Fig. S10. DFT calculations of IS, TS, and FS for water dissociation on β-Ni(OH)$_2$. Grey balls: Ni atoms; Red balls: O atoms; Pink balls: H atoms.
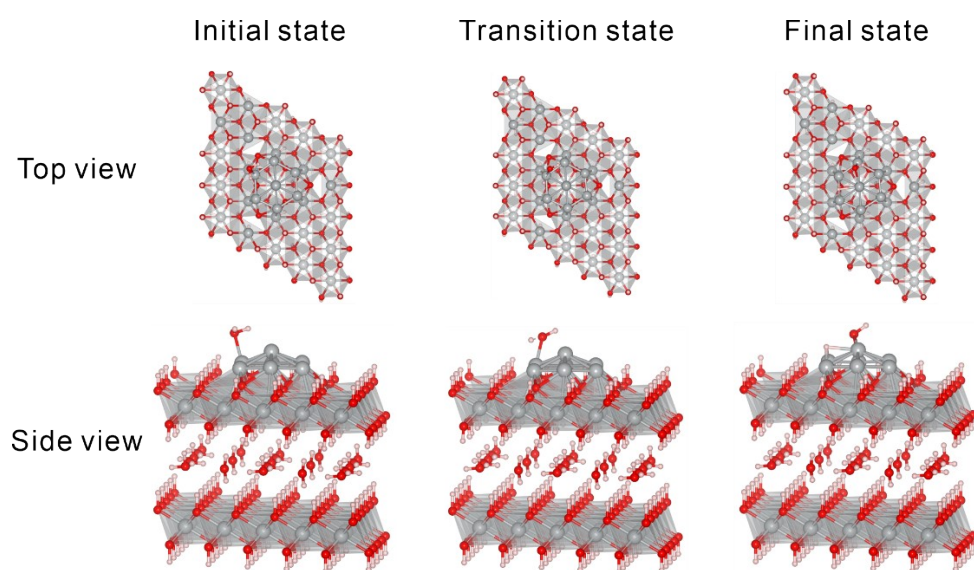
Fig. S11. DFT calculations of IS, TS, and FS for water dissociation on Ni/α-Ni(OH)$_2$. Grey balls: Ni atoms; Red balls: O atoms; Pink balls: H atoms.
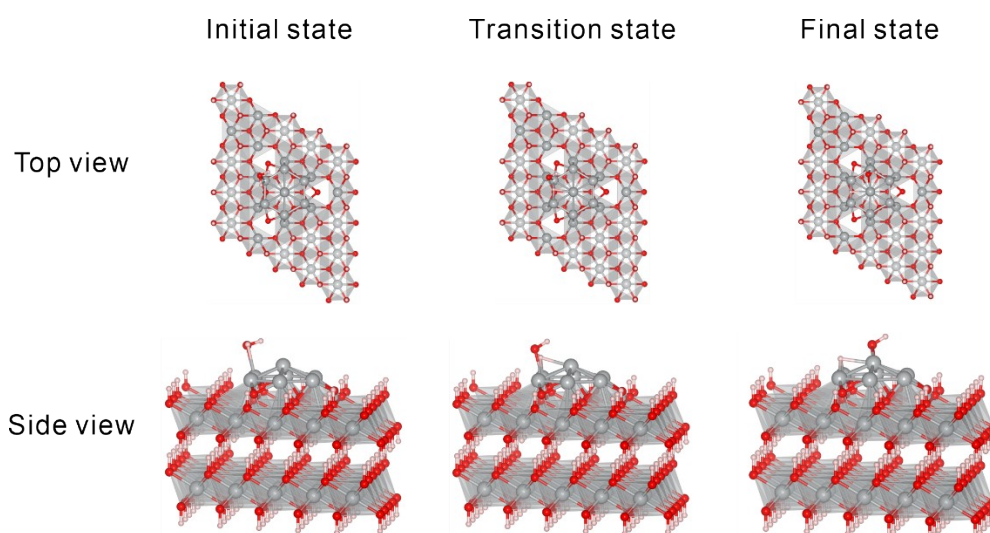
Fig. S12. DFT calculations of IS, TS, and FS for water dissociation on Ni/β-Ni(OH)$_2$. Grey balls: Ni atoms; Red balls: O atoms; Pink balls: H atoms.
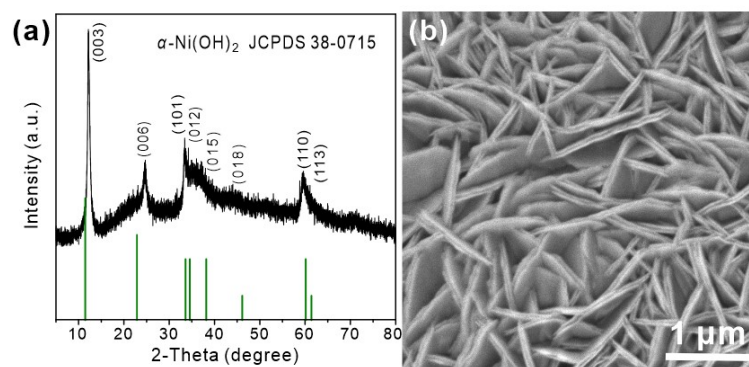
Fig. S13. (a) XRD pattern and (b) SEM image of α-Ni(OH)$_2$ NSAs.
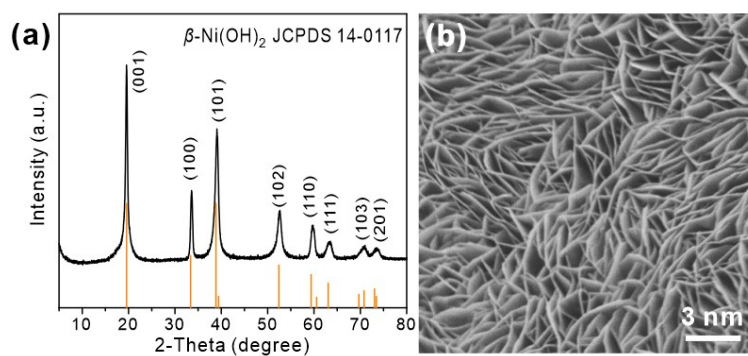
Fig. S14. (a) XRD pattern and (b) SEM image of β-Ni(OH)$_2$ NSAs.
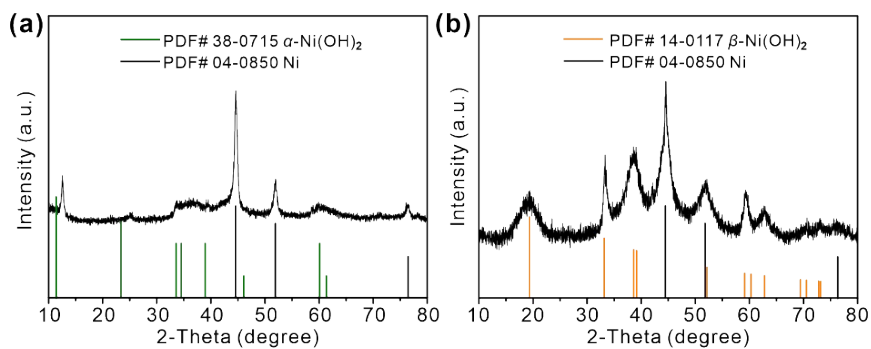
Fig. S15. XRD patterns of (a) Ni/α-Ni(OH)$_2$ NSAs and (b) Ni/β-Ni(OH)$_2$ NSAs.
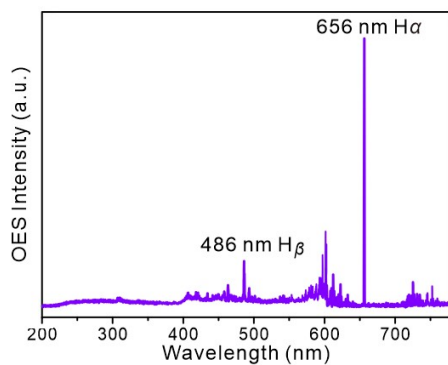
Fig. S16. Optical emission spectra of H$_2$ plasma.
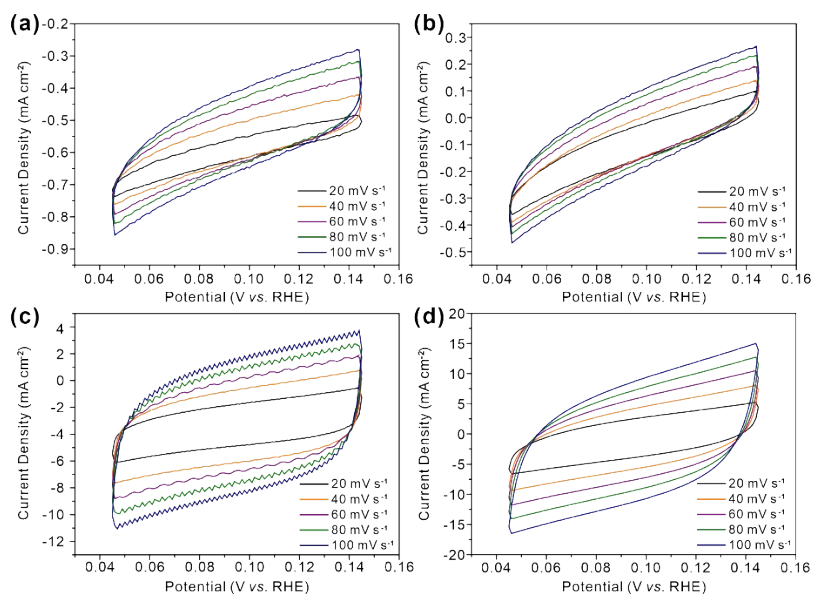
Fig. S17. CV curves of (a) α-Ni(OH)$_2$, (b) β-Ni(OH)$_2$, (c) Ni/α-Ni(OH)$_2$, and (d) Ni/β-Ni(OH)$_2$ NSAs in the double layer capacitive region at different scan rates.
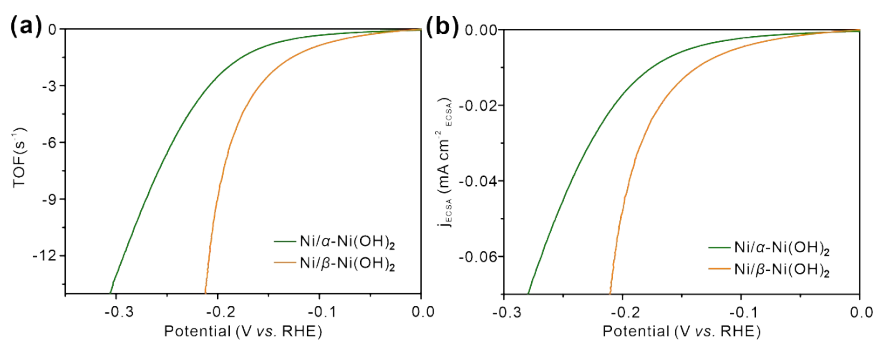
Fig. S18. (a) TOF curves and (b) ECSA normalized LSV curves of Ni/α-Ni(OH)$_2$ and Ni/β-Ni(OH)$_2$ NSAs.
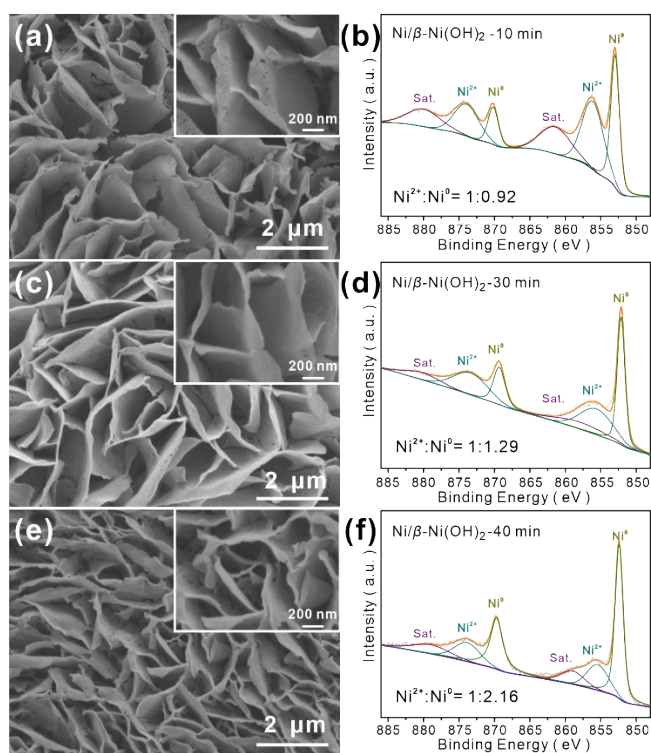
Fig. S19. (a,c,e) SEM images and (b,d,f) Ni 2p high-resolution XPS spectra of Ni/β-Ni(OH)$_2$-10 min (a,b), Ni/β-Ni(OH)$_2$-30 min (c,d), and Ni/β-Ni(OH)$_2$-40 min (e,f) NSAs.
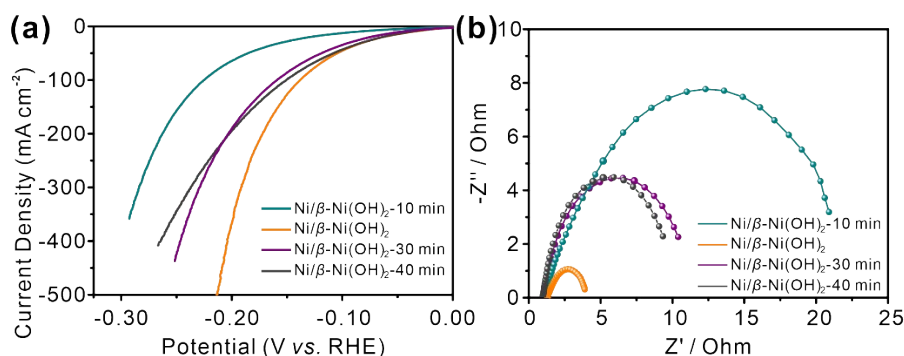
Fig. S20. (a) LSV curves and (b) Nyquist plots of Ni/β-Ni(OH)$_2$-10 min, Ni/β-Ni(OH)$_2$, Ni/β-Ni(OH)$_2$-30 min, and Ni/β-Ni(OH)$_2$-40 min NSAs. As can be seen, the Ni/β-Ni(OH)$_2$ NSAs obtained with plasma reduction time of 20 min demonstrate higher activity and smaller charge-transfer resistance than other samples.
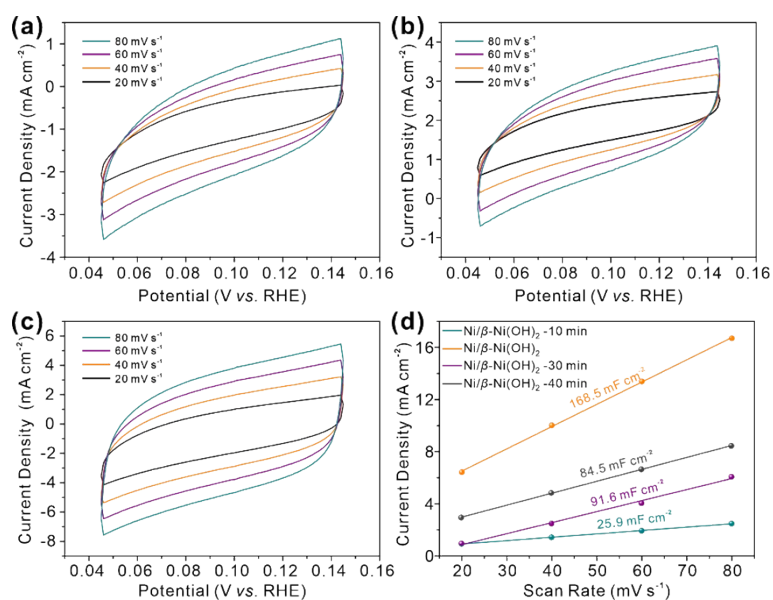
Fig. S21. CV curves of (a) Ni/β-Ni(OH)$_2$-10 min, (b) Ni/β-Ni(OH)$_2$-30 min, and (c) Ni/β-Ni(OH)$_2$-40 min NSAs at different scan rates. (d) Current density differences plotted against scan rates of Ni/β-Ni(OH)$_2$-10 min, Ni/β-Ni(OH)$_2$, Ni/β-Ni(OH)$_2$-30 min, and Ni/β-Ni(OH)$_2$-40 min NSAs. The higher C$_{dl}$ of Ni/β-Ni(OH)$_2$ NSAs demonstrate that they expose more active sites.
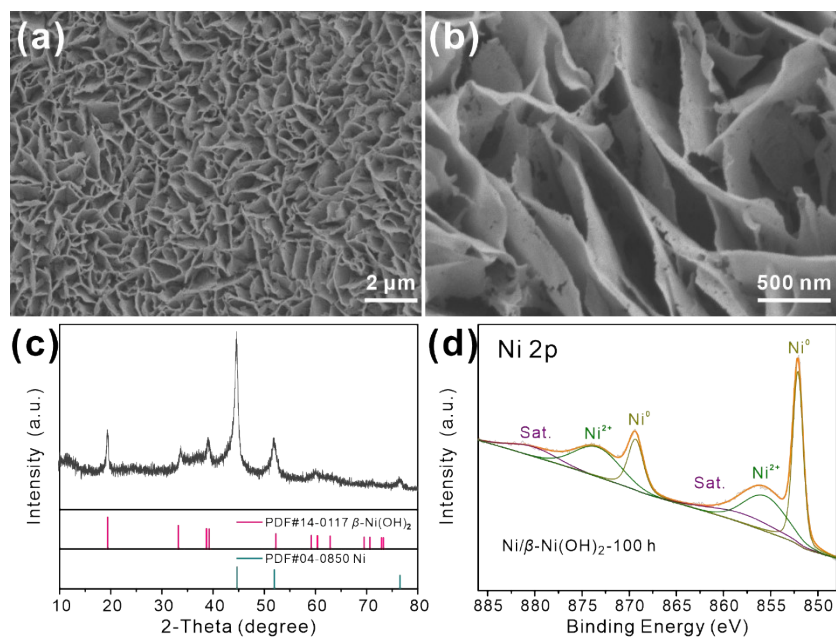
Fig. S22. (a-b) SEM images, (c) XRD pattern, and (d) Ni 2p XPS spectra of Ni/β-Ni(OH)$_2$ NSAs after 100 h of HER.
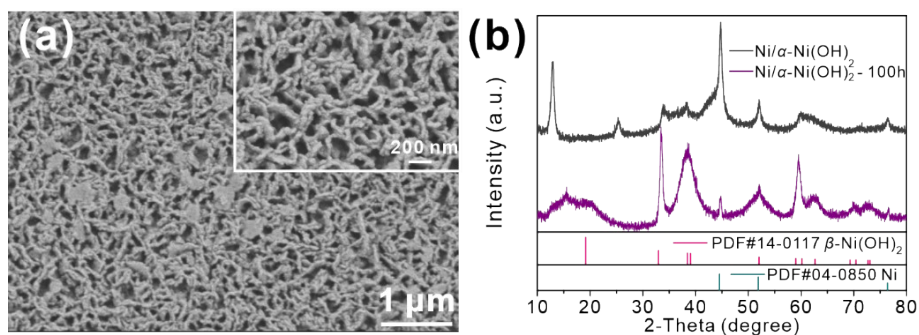
Fig. S23. (a) SEM images and (b) XRD patterns of Ni/α-Ni(OH)$_2$ NSAs before and after 100 h of HER.
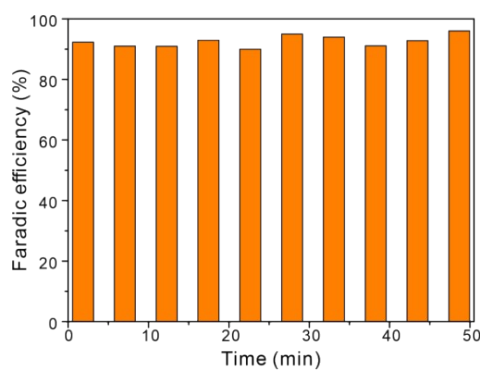
Fig. S24. FE for hydrogen evolution on Ni/β-Ni(OH)$_2$ NSAs as a function of time at the current density of 10 mA cm^{-2}.
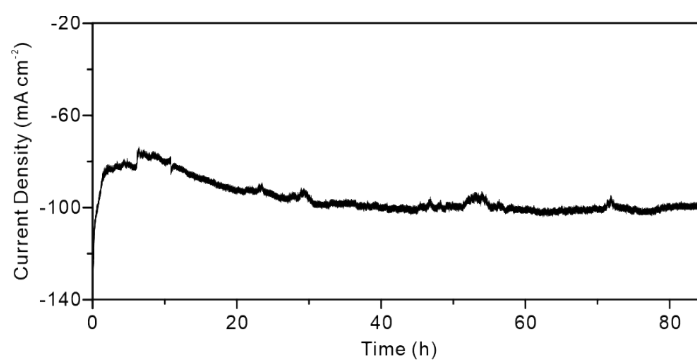
Fig. S25. HER stability test of Ni/β-Ni(OH)$_2$ NSAs in 1.0 M KOH seawater.
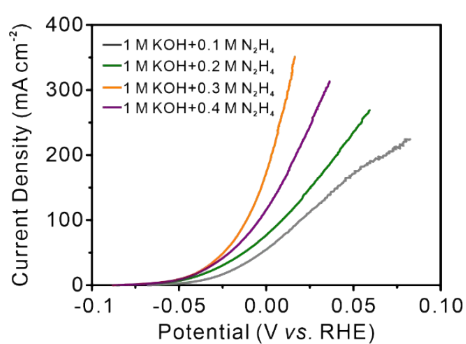
Fig. S26. LSV curves of Ni/β-Ni(OH)$_2$ NSAs with different concentrations of hydrazine.
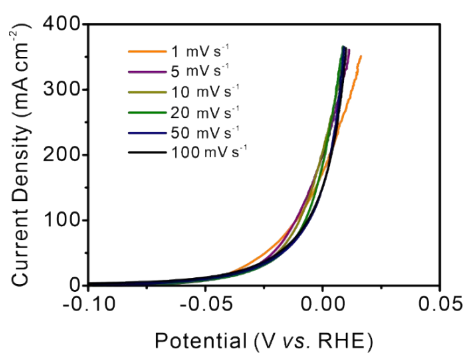
Fig. S27. LSV curves of Ni/β-Ni(OH)$_2$ NSAs at different scan rates.
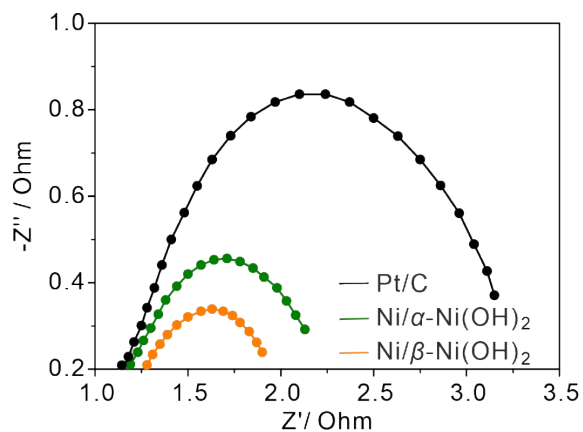
Fig. S28. The Nyquist plots of Ni/α-Ni(OH)$_2$ NSAs, Ni/β-Ni(OH)$_2$ NSAs, and Pt/C in 1.0 M KOH + 0.3 M N$_2$H$_4$.
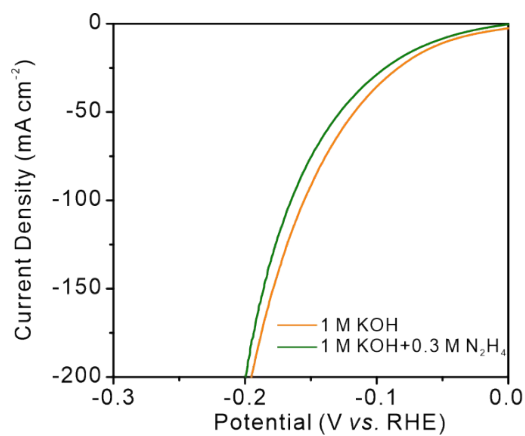
Fig. S29. LSV curves of Ni/β-Ni(OH)$_2$ NSAs in 1.0 M KOH and 1.0 M KOH + 0.3 M N$_2$H$_4$.
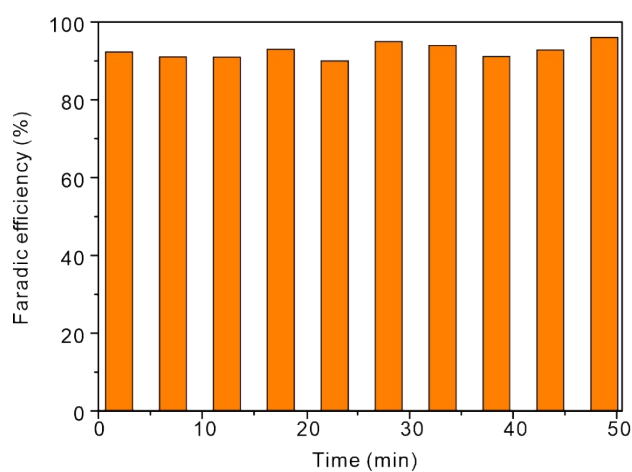
Fig. S30. FE for hydrogen evolution on Ni/β-Ni(OH)$_2$ NSAs as a function of time at the current density of 10 mA cm^{-2} during OHzS.
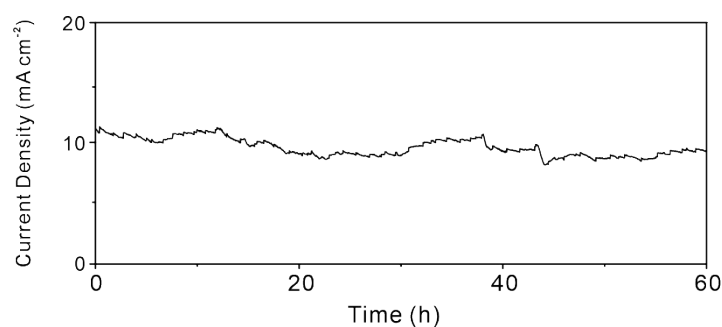
Fig. S31. Chronoamperometric curve of Ni/β-Ni(OH)$_2$ NSAs for OHzS in alkaline seawater with 1.0 M KOH and 0.3 M N$_2$H$_4$.
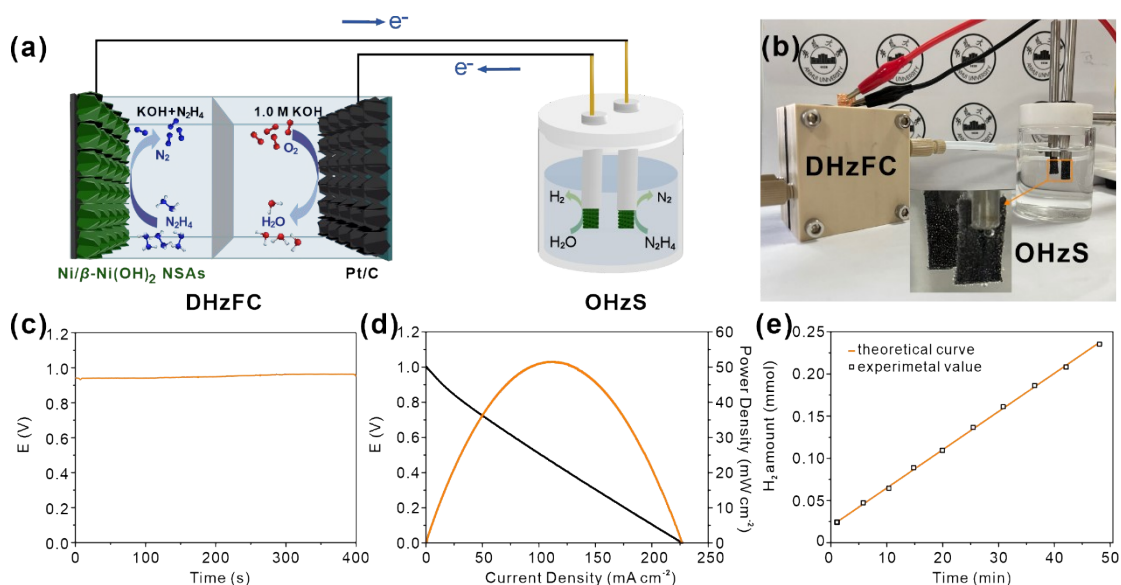
Fig. S32. (a) Schematic illustration and working principle of DHzFC. (b) Optical image of the integrated H$_2$ production system. (c) Open-circuit voltage of the homemade DHzFC. (d) Discharge polarization curve and power density plot of DHzFC. (e) The H$_2$ generation rate of the self-powered H$_2$ production system in 1.0 M KOH with 0.3 M hydrazine.

Table S1. The atomic ratio of Ni^{2+} : Ni^0 in Ni/Ni(OH)$_2$.

Samples	The ratio of Ni^{2+} : Ni^0
Ni/α-Ni(OH)$_2$ NSAs	1:1.18
Ni/β-Ni(OH)$_2$ NSAs	1:1.27
Ni/β-Ni(OH)$_2$-10 min NSAs	1:0.92
Ni/β-Ni(OH)$_2$-30 min NSAs	1:1.79
Ni/β-Ni(OH)$_2$-40 min NSAs	1:2.16

Table S2. Comparison of the HER performance of Ni/β-Ni(OH)$_2$ NSAs with other reported HER electrocatalysts in 1 M KOH electrolyte.

Electrocatalysts	j (mA cm^{-2})	Overpotential (mV) at corresponding j	References
Ni/β-Ni(OH)$_2$	**10**	**58**	**This work**
	100	**157**	
Ni/Ni(OH)$_2$/NF	10	72	[S8]
	100	233	
Ni(OH)$_2$-Ni$_3$N	20	112	[S9]
	100	190	
NiO/Ni-CNT	10	80	[S10]
Ni(OH)$_2$/MoS$_2$	10	150	[S11]
Ni(OH)$_2$-Fe$_2$P/Ti mesh	10	76	[S12]
Ni/NiO	10	145	[S13]
Fe-Ni(OH)$_2$	10	138	[S14]
Ni/NiO@C NPs	10	64	[S15]
Ni(OH)$_2$	10	>355 mV	[S16]

Table S3. Comparison of the HER performance of Ni/β-Ni(OH)$_2$ NSAs with other reported HER electrocatalysts in 1 M KOH seawater electrolyte.

Electrocatalysts	j (mA cm^{-2})	Overpotential (mV) at corresponding j	References
Ni/β-Ni(OH)$_2$	**10**	**62**	**This work**
	100	**179**	
Ni-N$_3$	10	139	[S17]
S-NiMoO$_4$@NiFe-LDH/NF	100	220	[S18]
Co-Ni$_2$P	50	115	[S19]
CoNiSe$_2$/N-SSCSs	10	88	[S20]
Ni$_5$P$_4$@Ni$^{2+\delta}$O$_\delta$(OH)$_{2-\delta}$	10	144	[S21]

References

(1) Kresse, G.; Hafner, J. Ab Initio Molecular Dynamics for Liquid Metals. *Phys. Rev. B* **1993**, *47*, 558-561.

(2) Kresse, G.; Furthmüller, J. Efficient Iterative Schemes for Ab Initio Total-Energy Calculations Using a Plane-Wave Basis Set. *Phys. Rev. B* **1996**, *54*, 11169-11186.

(3) Kresse, G.; Furthmüller, J. Efficiency of Ab-Initio Total Energy Calculations for Metals and Semiconductors Using a Plane-Wave Basis Set. *Comput. Mater. Sci.* **1996**, *6*, 15-50.

(4) Blöchl, P. E. Projector Augmented-Wave Method. *Phys. Rev. B* **1994**, *50*, 17953-17979.

(5) Kresse, G.; Joubert, D. From Ultrasoft Pseudopotentials to the Projector Augmented-Wave Method. *Phys. Rev. B* **1999**, *59*, 1758-1775.

(6) Perdew, J. P.; Wang, Y. Accurate and Simple Analytic Representation of the Electron-Gas Correlation Energy. *Phys. Rev. B* **1992**, *45*, 13244-13249.

(7) Perdew, J. P.; Burke, K.; Ernzerhof, M. Generalized Gradient Approximation Made Simple. *Phys. Rev. Lett.* **1996**, *77*, 3865-3868.

(8) Zhong, W.; Li, W.; Yang, C.; Wu, J.; Zhao, R.; Idrees, M.; Xiang, H.; Zhang, Q.; Li, X. Interfacial Electron Rearrangement: Ni Activated Ni(OH)$_2$ for Efficient Hydrogen Evolution. *J. Energy Chem.* **2021**, *61*, 236-242.

(9) Gao, M.; Chen, L.; Zhang, Z.; Sun, X.; Zhang, S. Interface Engineering of the Ni(OH)$_2$–Ni$_3$N Nanoarray Heterostructure for the Alkaline Hydrogen Evolution Reaction. *J. Mater. Chem. A* **2018**, *6*, 833-836.

(10) Gong, M.; Zhou, W.; Tsai, M.-C.; Zhou, J.; Guan, M.; Lin, M.-C.; Zhang, B.; Hu, Y.; Wang, D.-Y.; Yang, J.; Pennycook, S. J.; Hwang, B.-J.; Dai, H. Nanoscale Nickel Oxide/Nickel Heterostructures for Active Hydrogen Evolution Electrocatalysis. *Nat.*

Commun. **2014**, *5*, 4695.

(11) Zhao, G.; Lin, Y.; Rui, K.; Zhou, Q.; Chen, Y.; Dou, S. X.; Sun, W. Epitaxial Growth of Ni(OH)$_2$ Nanoclusters on MoS$_2$ Nanosheets for Enhanced Alkaline Hydrogen Evolution Reaction. *Nanoscale* **2018**, *10*, 19074-19081.

(12) Zhang, X.; Zhu, S.; Xia, L.; Si, C.; Qu, F.; Qu, F. Ni(OH)$_2$–Fe$_2$P Hybrid Nanoarray for Alkaline Hydrogen Evolution Reaction with Superior Activity. *Chem. Commun.* **2018**, *54*, 1201-1204.

(13) Yan, X.; Tian, L.; Chen, X. Crystalline/Amorphous Ni/NiO Core/Shell Nanosheets as Highly Active Electrocatalysts for Hydrogen Evolution Reaction. *J. Power Sources* **2015**, *300*, 336-343.

(14) Ren, J.-T.; Yuan, G.-G.; Weng, C.-C.; Chen, L.; Yuan, Z.-Y. Uniquely Integrated Fe-doped Ni(OH)$_2$ Nanosheets for Highly Efficient Oxygen and Hydrogen Evolution Reactions. *Nanoscale* **2018**, *10*, 10620-10628.

(15) Yin, J.; Fan, Q.; Li, Y.; Cheng, F.; Zhou, P.; Xi, P.; Sun, S. Ni–C–N Nanosheets as Catalyst for Hydrogen Evolution Reaction. *J. Am. Chem. Soc.* **2016**, *138*, 14546-14549.

(16) Luo, J.; Im, J.-H.; Mayer, M. T.; Schreier, M.; Nazeeruddin, M. K.; Park, N.-G.; Tilley, S. D.; Fan, H. J.; Grätzel, M. Water Photolysis at 12.3% Efficiency Via Perovskite Photovoltaics and Earth-Abundant Catalysts. *Science* **2014**, *345*, 1593-1596.

(17) Zang, W.; Sun, T.; Yang, T.; Xi, S.; Waqar, M.; Kou, Z.; Lyu, Z.; Feng, Y. P.; Wang, J.; Pennycook, S. J. Efficient Hydrogen Evolution of Oxidized Ni-N$_3$ Defective Sites for Alkaline Freshwater and Seawater Electrolysis. *Adv. Mater.* **2021**, *33*, 2003846.

(18) Wang, H.; Chen, L.; Tan, L.; Liu, X.; Wen, Y.; Hou, W.; Zhan, T. Electrodeposition of NiFe-Layered Double Hydroxide Layer on Sulfur-Modified Nickel Molybdate Nanorods for Highly Efficient Seawater Splitting. *J. Colloid Interface Sci.* **2022**, *613*, 349-358.

(19) Sun, X.; Yang, P.; Wang, S.; Hu, J.; Chen, P.; Xing, H.; Zhu, W. Synthesis of Bristlegrass-Like Co-doped Ni$_2$P Composites on Ni Foam for Overall Seawater Splitting. *Int. J. Hydrogen Energy* **2022**, *6*, 194.

(20) Wang, Z.; Tian, Y.; Wen, M.; Wu, Q.; Zhu, Q.; Fu, Y. Integrating CoNiSe$_2$ Nanorod-Arrays onto N-doped Sea-Sponge-C Spheres for Highly Efficient Electrocatalysis of Hydrogen Evolution Reaction. *Chem. Eng. J.* **2022**, *446*, 137335.

(21) Huang, Y.; Hu, L.; Liu, R.; Hu, Y.; Xiong, T.; Qiu, W.; Balogun, M. S.; Pan, A.; Tong, Y. Nitrogen Treatment Generates Tunable Nanohybridization of Ni$_5$P$_4$ Nanosheets with Nickel Hydr(oxy)Oxides for Efficient Hydrogen Production in Alkaline, Seawater and Acidic Media. *Appl. Catal., B* **2019**, *251*, 181-194.